Macrocrack–Microcrack Configurations Under Impact Loading

CH. ZHANG*

*Department of Civil Engineering, Northwestern University, Evanston,
IL 60208, USA*

ABSTRACT

The interaction of a stress pulse with configurations of a macrocrack and a
neighboring microcrack is investigated. A time-domain boundary integral
equation (BIE) method has been applied to obtain time histories of the
dynamic stress intensity factors. Parametrical studies show the effects of
the microcrack on the pulse-generated crack-tip fields of the macrocrack.

KEYWORDS

Macrocrack-microcrack configurations; near-tip fields; dynamic
loads

INTRODUCTION

This paper deals with the investigation of elastodynamic crack-tip fields
generated by the interactions of a pulse with a macrocrack and a neighboring
microcrack, as shown in Fig. 1. Macrocrack-microcrack configurations are
often observed in brittle materials such as ceramics, rocks and concretes.
In such solids the high level of stress and deformation in the vicinity of a
crack tip gives rise to microcracking and/or the formation of microvoids in
a confined zone surrounding the macrocrack tip. The existence of
neighboring microcracks may significantly alter the stress intensity at the
main crack tip. Depending on the size and location of microcracks or
microvoids, their presence can either increase the stress intensity factors
(stress amplification) or decrease it (stress shielding or toughening).
Knowledge of the dependence of the stress intensity factors on the
microdefects will assist in predicting macrocrack propagation. For static

*Permanent address: Department of Engineering Mechanics, Tongji University,
Shanghai, P.R. China

loading several results can be found in the literature. For dynamic loading the effects of microcracks on the macrocrack have not yet been investigated in detail.

A time-domain boundary integral equation (BIE) method has been applied to obtain time histories of elastodynamic stress intensity factors for the macrocrack. Parametrical studies show the influence of the size and location of the microcrack on the effective stress intensity factors of the macrocrack. Particular attention has been devoted to dynamic overshoots of the stress intensity factors. For step-stress pulses the dynamic overshoot phenomenon has been noted in [1]-[2].

FORMULATION

Two configurations of an unbounded, homogeneous, isotropic, linearly elastic body containing a macro-crack and a neighboring micro-crack are shown in Fig. 1. An incident stress pulse of the form
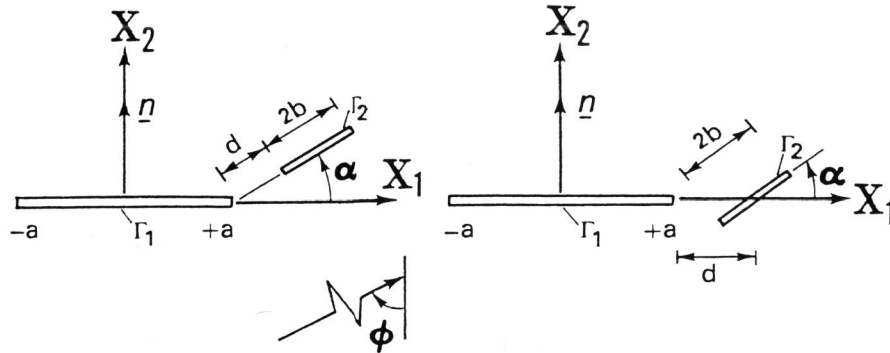

Fig. 1: Macrocrack-microcrack configurations

$$\sigma_{\alpha\beta}^{in}(\underline{x},t) = \bar{\sigma}_{\alpha\beta}H[c_L t - (x_1 + a)\sin\phi - x_2\cos\phi] \qquad (2.1a)$$

interacts with the two cracks, and generates a scattered field. Here

$$\bar{\sigma}_{\alpha\beta} = \begin{bmatrix} \lambda + 2\mu - 2\mu\cos^2\phi & \mu\sin(2\phi) \\ \mu\sin(2\phi) & \lambda + 2\mu - 2\mu\sin^2\phi \end{bmatrix} , \qquad (2.1b)$$

where λ and μ are Lamé's elastic constants, and ϕ denotes the angle of incidence. Also $H[\cdot]$ denotes the Heaviside step function and $c_L = \sqrt{(\lambda+2\mu)/\rho}$ is the velocity of longitudinal waves. The propagation direction of the incident pulse is in the x_1x_2-plane, and the analysis of this paper is two-dimensional and for a state of plane strain. In terms of the incident field, $\sigma_{\alpha\beta}^{in}(\underline{x},t)$, and the scattered field, $\sigma_{\alpha\beta}^{sc}(\underline{x},t)$, the total stress field may be written as

$$\sigma_{\alpha\beta}(\underline{x},t) = \sigma_{\alpha\beta}^{in}(\underline{x},t) + \sigma_{\alpha\beta}^{sc}(\underline{x},t), \quad \alpha,\beta = 1,2. \qquad (2.2)$$

Since the faces of the cracks are free of tractions, the following conditions follow for the scattered field

$$f_\alpha^{sc}(\underline{x},t) = - f_\alpha^{in}(\underline{x},t) \quad \text{for} \quad \underline{x} \in \Gamma_1 + \Gamma_2 , \qquad (2.3)$$

where $f_\alpha = \sigma_{\alpha\beta}n_\beta$ denote the traction components, and Γ_1 and Γ_2 define the faces of the macrocrack and the microcrack, respectively. The initial conditions for the scattered displacement field are

$$u_\alpha^{sc}(\underline{x},t) = \dot{u}_\alpha^{sc}(\underline{x},t) = 0 \quad \text{for } t < 0. \qquad (2.4)$$

The integral representation for the components of the scattered stress may be written as

$$\sigma_{\alpha\beta}^{sc}(\underline{x}_p,t) = - \int_0^t \int_\Gamma K_{\alpha\beta\delta\epsilon}^G(\underline{x}_p,t;\underline{x},\tau)\Delta u_\delta(\underline{x},\tau)n_\epsilon \, ds d\tau, \quad \underline{x}_p \notin \Gamma , \qquad (2.5)$$

where n_ϵ are the components of the normal vector to $\Gamma = \Gamma_1 + \Gamma_2$, and

$$K_{\alpha\beta\delta\epsilon}^G = \lambda\delta_{\alpha\beta}\sigma_{\delta\epsilon\gamma,\gamma}^G + \mu(\sigma_{\delta\epsilon\alpha,\beta}^G + \sigma_{\delta\epsilon\beta,\alpha}^G) . \qquad (2.6)$$

Equation (2.5) yields a set of BIE's by using $f_\alpha = \sigma_{\alpha\beta}n_\beta$ and by taking $\underline{x}_p \to \Gamma$. Unfortunately, such BIE's are hyper singular when the observation point $\underline{x}_p$ and the source point $\underline{x}$ coincide [3],[4]. To reduce the high singularities a regularization procedure has been developed which results in the following discretized BIE's [4]

$$f_\alpha^{in}(\underline{x}_p,t) = n_\beta(\underline{x}_p) \sum_{j=1}^J \int_0^t \left\{ H_{\alpha\beta\delta}^1 \Delta u_\delta \Big|_{s_j}^{s_{j+1}} - \int_{s_j}^{s_{j+1}} H_{\alpha\beta\delta\epsilon}^1 \lambda_\mu \Delta u_{\delta,\lambda} n_\mu \, ds \right.$$
$$\left. + \rho \int_{s_j}^{s_{j+1}} H_{\alpha\beta\delta}^2 \Delta\ddot{u}_\delta dS \right\} d\tau , \qquad (2.7)$$

in which s_j and s_{j+1} are the endpoints of the j-th element, $\epsilon_{\lambda\mu}$ is the two-dimensional permutation tensor, and

$$H_{\alpha\beta\delta}^1 = \lambda\delta_{\alpha\beta}\epsilon_{\gamma\epsilon}\sigma_{\delta\epsilon\gamma}^G + \mu(\epsilon_{\beta\epsilon}\sigma_{\delta\epsilon\alpha}^G + \epsilon_{\alpha\epsilon}\sigma_{\delta\epsilon\beta}^G) , \qquad (2.8)$$

$$H_{\alpha\beta\delta}^2 = \lambda\delta_{\alpha\beta}u_{\delta\gamma}^G n_\gamma + \mu(u_{\delta\alpha}^G n_\beta + u_{\delta\beta}^G n_\alpha) , \qquad (2.9)$$

where $u_{\delta\gamma}^G$ and $\sigma_{\delta\epsilon\gamma}^G$ denote the elastodynamic Green's functions. It should be noted here that the singular terms in the simplified BIE's (2.7) can be integrated numerically and analytically without difficulties.

NUMERICAL IMPLEMENTATION

To solve the BIE's (2.7) discretization of time t is necessary. Here we have used equal time increments Δt, where $t_n = n\Delta t$ (n = 1,2,···N) denotes the time after the n-th time-step. The unknown crack opening displacements $\Delta u_\alpha(\underline{x},\tau)$ in (2.7) are approximated by the following interpolation functions

$$\Delta u_\alpha(\underline{x},\tau) = \sum_j \sum_n \mu_j(\underline{x})\eta^n(\tau)(\Delta u_\alpha)_j^n . \qquad (3.1)$$

In our analysis the function $\mu_j(\underline{x})$ has been taken to be unity over each element except for elements near crack tips. For these elements a special shape function

$$\mu_j(\underline{x}) = (a + x_1)^{1/2} \qquad (3.2)$$

is used to describe the proper behavior of Δu_α at the crack tips $x_1 = \pm a$. Higher order shape functions for $\eta^n(\tau)$ are desirable since Eq.(2.7) contains not only the functions Δu_α, but also their derivatives. In this paper the piecewise linear shape function

$$\eta^n(\tau) = \begin{cases} 1 - \dfrac{|\tau - n\Delta t|}{\Delta t} & , \; |\tau - n\Delta t| \leq \Delta t \; , \\ 0 & , \; \text{otherwise} \; , \end{cases} \tag{3.3}$$

is employed.

For each time-step Eq.(2.7) can be rewritten as

$$f_\alpha^{in}(\underline{x}_P, t_m) = n_\beta(\underline{x}_P) \sum_{n=1}^{N} \sum_{j=1}^{J} \left[L_{\alpha\beta\delta}^{mn}(\underline{x}_P;\underline{x})\mu_j(\underline{x}) \Big|_{s_j}^{s_{j+1}} \right.$$

$$- \int_{s_j}^{s_{j+1}} L_{\alpha\beta\delta}^{mn}(\underline{x}_P;\underline{x}) \frac{\partial}{\partial x_\lambda} \mu_j(\underline{x}) \epsilon_{\lambda\mu} n_\mu \, ds$$

$$\left. + \rho \int_{s_j}^{s_{j+1}} M_{\alpha\beta\delta}^{mn}(\underline{x}_P;\underline{x})\mu_j(\underline{x})ds \right] (\Delta u_\delta)_j^n \; . \tag{3.4}$$

In these equations the following abbreviations have been used for convenience

$$L_{\alpha\beta\gamma}^{mn}(\underline{x}_P;\underline{x}) = \int_{(n-1)\Delta t}^{(n+1)\Delta t} H_{\alpha\beta\gamma}^1(\underline{x}_P, t_m;\underline{x},\tau)\eta^n(\tau)d\tau \; , \tag{3.5}$$

$$M_{\alpha\beta\gamma}^{mn}(\underline{x}_P;\underline{x}) = \int_{(n-1)\Delta t}^{(n+1)\Delta t} H_{\alpha\beta\gamma}^2(\underline{x}_P, t_m;\underline{x},\tau)\ddot{\eta}^n(\tau)d\tau \; . \tag{3.6}$$

With Eq.(3.3), the time integrations in (3.5) and (3.6) can be performed analytically. For details see Reference [4].

By choosing J collocation points on Γ and N points for t, and requiring that Eqs.(3.4) are satisfied at each discrete point x_P^i (i = 1,2,$\cdots$J), we obtain a system of linear algebraic equations which has been solved numerically at each time $t_m = m\Delta t$ (m = 1,2,$\cdots$N). Spatial integrations of regular terms in (3.4) have been performed numerically by using an 8-points Gaussian quadrature formula for the constant shape function, and by using an 8-points Gauss-Jacobian formula for the "crack-tip" shape function. The singular terms have been integrated analytically and numerically.

RESULTS

The dynamic stress intensity factors can be calculated by using the following well-known relations

$$\begin{Bmatrix} K_I^\pm(t) \\ K_{II}^\pm(t) \end{Bmatrix} = \frac{\mu\sqrt{2\pi}}{4(1-\nu)} \lim_{x_1 \to \pm a} \frac{1}{(a \mp x_1)^{1/2}} \begin{Bmatrix} \Delta u_2(x_1,t) \\ \Delta u_1(x_1,t) \end{Bmatrix} \; , \tag{4.1}$$

once the crack opening displacements have been calculated by the numerical scheme described in the last section. In Eq.(4.1), "+" indicates the tip at

$x_1 = a$ and "-" indicates the tip at $x_1 = -a$, while ν denotes Poisson's ratio.

All calculations have been carried out for a Poisson's ratio $\nu = 1/4$. The geometrical configuration is shown in Fig. 1. The principal (macro) crack has been discretized into 50 elements of equal length, and a proportional number of elements have been used for the microcrack.

For $b/a = 0$, the configuration reduces to a single crack of length 2a. This case was used to check numerical results obtained by our method. The agreements with Thau and Lu's results [2] was found to be very good. The time increment was selected as $c_T\Delta t = 0.08a$. The influence of Δt on the stability of the time-stepping scheme has been studied numerically, and it was found that too small a value of Δt may cause instabilities at large time. The same conclusions have been drawn by Nishimura et al.[3]. The time increment chosen here always yielded good results, at least in the time interval considered here (100 time-steps).

For $b/a = 0.1$, $d/a = 0.015$, and for normal incidence, $\phi = 0^\circ$, the dynamic stress intensity factors are shown in Figures 2a,b,c versus the dimensionless time $c_L t/a$, for various values of the angle of crack inclination, α. All results have been normalized by the static stress intensity factors of a single macrocrack under the corresponding static load. Figure 2a shows that, as expected, the presence and orientation of a microcrack do not influence the left tip of the macrocrack at small time.

However, after $c_L t/a \simeq 3$ the difference in $\overline{K}_I^-$ becomes somewhat distinct. It is, however, evident that the crack-tip away from the microcrack is not significantly affected by the presence of the microcrack. The contribution of the inclined microcrack to the $\overline{K}_{II}^-$-factor is also negligibly small in the sense that $\overline{K}_{II}^- < 2\%$, and the results are not shown here. The presence of the microcrack, does, however, give rise to a substantial increase of the Mode-I stress intensity factor at the tip adjoining the microcrack (Fig. 2b). The $\overline{K}_I^+$-factor decreases with increasing inclination angle α, while a complicated dependence of the $\overline{K}_{II}^+$-factor on α is noted (Fig. 2c). At both tips of the main crack, the maximum dynamic stress intensity factors exceed the corresponding static values, which are reached at large time t.

Figures 3a,b,c show the normalized dynamic stress intensity factors for the configuration depicted in Fig. 1b., for normal incidence of a stress pulse, $\phi = 0^\circ$. The geometrical parameters are $b/a = 0.1$, $d/a = 0.115$. The time histories of $\overline{K}_I^-$ (Fig. 3a) for various α are very similar to those shown in Fig. 2a. Again $\overline{K}_{II}^-$ is very small. The amplification in $\overline{K}_I^+$-factors increases with decreasing α. Maximum dynamic overshoots of $\overline{K}_I^+$ are induced for the collinear crack configuration ($\alpha = 0^\circ$), while the presence of a slightly inclined microcrack (for example $\alpha = 20^\circ$) gives rise to a larger $\overline{K}_{II}^+$ value.

The dependence of the dynamic stress intensity factors on the distance of the crack tips and the size of the microcrack has been investigated for collinear cracks, again for normal incidence. For a fixed half-length of the microcrack, $b/a = 0.1$, and for various crack-tip distances, d/a, the time history of the normalized dynamic stress intensity factors is presented in Figs. 4a,b. Due to symmetry with respect to $x_2 = 0$, the Mode-II stress

intensity factors are identically zero, $\overline{K}_{II}^{\pm} = 0$. The variation of $\overline{K}_I^-$ (Fig. 4a) with d/a is fairly smooth, since the left tip of the macrocrack is less affected by the microcrack. The Mode-I stress intensity factor of the crack tip adjoining the microcrack, $\overline{K}_I^+$, increases, however, substantially with decreasing crack-tip distance d/a, as shown in Fig. 4b. Considerable amplifications in $\overline{K}_I^+$ occur for very small values of d/a. Both $\overline{K}_I^+$ and $\overline{K}_I^-$, assume the values for a single solitary crack of half-length a as d/a $\to^I_\infty$.

Finally, the dependence of the normalized stress intensity factors on the dimensionless half-length of the microcrack, b/a, is shown in Figures 5a,b. Results are presented for two collinear cracks with d/a = 0.05, and for $\phi = 0^\circ$. The peak $\overline{K}_I^-$-factor increases with increasing b/a, but it is shifted to somewhat larger time $c_L t/a$. The $\overline{K}_I^-$-factor for larger b/a can be slightly smaller than for a shorter microcrack (smaller b/a), which is in contrast to the static case (see Yokobori et al.[5]). Figure 5b shows the variation of $\overline{K}_I^+$ with the microcrack size b/a. As expected, a larger microcrack gives rise to a larger amplification of the stress intensity factors.

ACKNOWLEDGEMENT

REFERENCES

[1] J.D. Achenbach, Dynamic Effects in Brittle Fracture, in Mechanics Today, 1, pp. 1-57. Pergamon, New York (1972).

[2] S.A. Thau and T.H. Lu, Transient Stress Intensity Factors for a Finite Crack in an Elastic Solid Caused by a Dilatational Wave, Int. J. Solids Structures, 7, 731-750 (1971).

[3] N. Nishimura, Q.C. Guo and S. Kobayashi, Boundary Integral Equation Methods in Elastodynamic Crack Problems, Proc. 9th Int. Conf. BEM, Vol 2 (Eds. W.L. Wendland and C.A. Brebbia), Springer-Verlag, pp. 279-291 (1987).

[4] Ch. Zhang and J.D. Achenbach, Time-Domain Boundary Element Analysis of Dynamic Near-Tip Fields for Impact-Loaded Collinear Cracks, submitted for publication.

[5] T. Yokobori, M. Ohashi and M. Ichikawa, The Interaction of two Collinear Asymmetric Elastic Cracks, Reports of the Research Institute for Strength and Fracture of Materials, Tohoku University, 1, 33-39 (1965).
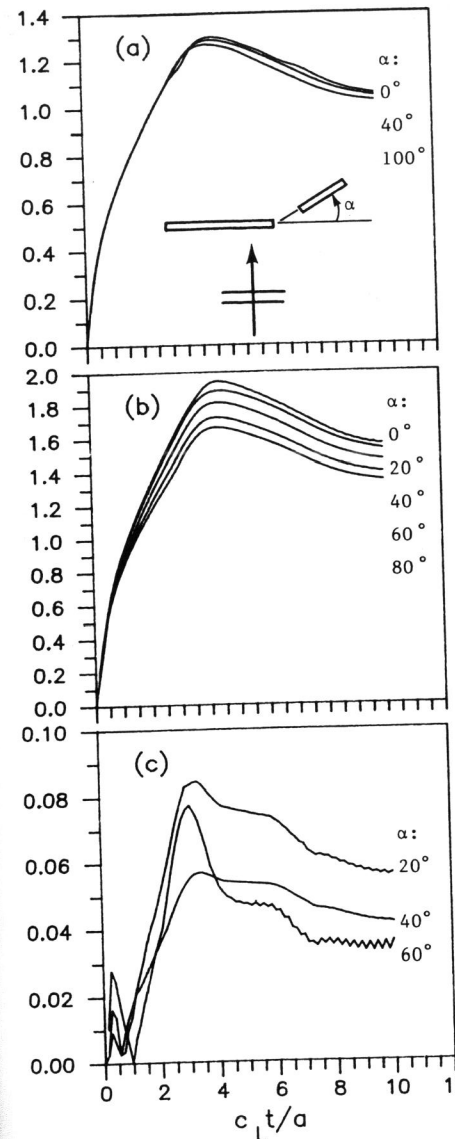
Fig. 2: Normalized stress intensity factors; (a) $\overline{K}_I^-$; (b) $\overline{K}_I^+$; (c) $\overline{K}_{II}^+$.
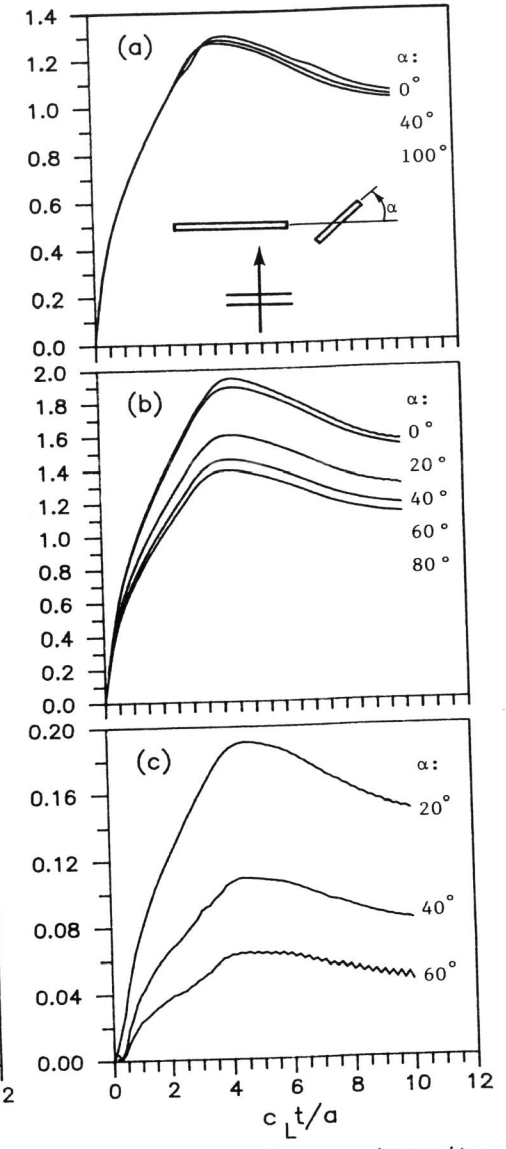
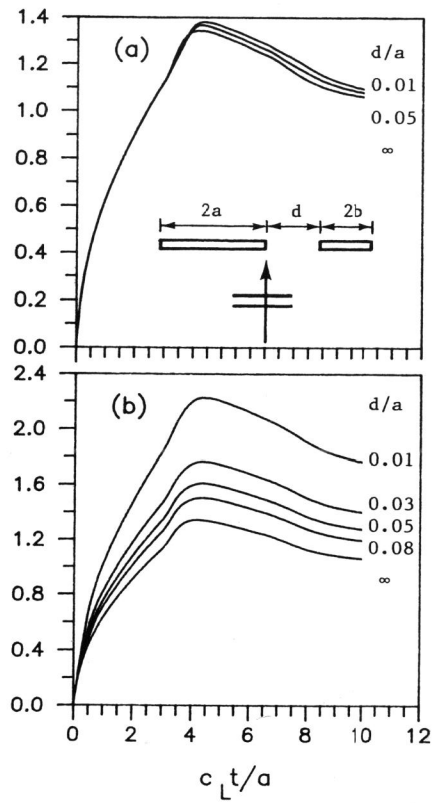Fig. 3: Normalized stress intensity factors; (a) $\overline{K}_I^-$; (b) $\overline{K}_I^+$; (c) $\overline{K}_{II}^+$.

Fig. 4: Normalized stress intensity factors; (a) $\overline{K}_I^-$; (b) $\overline{K}_I^+$.

Fig. 5: Normalized stress intensity factors; (a) $\overline{K}_I^-$; (b) $\overline{K}_I^+$.